Concentrated vertical jetting mechanism for isotropically focused ZnO/Si surface acoustic waves

M. Jangi,[1,*,#] J. T. Luo, [2,3,*] R. Tao,[2] J. Reboud,[4] R. Wilson,[4] J.M. Cooper,[4] D. Gibson,[5] Y.Q. Fu,[2,#]

[1] School of Mechanical Engineering, University of Birmingham, Edgbaston B15 2TT, Birmingham, UK

[2] Faculty of Engineering and Environment, University of Northumbria, Newcastle upon Tyne, NE1 8ST, UK

[3] Shenzhen Key Laboratory of Advanced Thin Films and Applications, College of Physics and Energy, Shenzhen University, Shenzhen, 518060, P.R. China

[4] Division of Biomedical Engineering, School of Engineering, University of Glasgow, Rankine Building, G12 8LT, Glasgow, UK

[5] Institute of Thin Films, Sensors & Imaging, Scottish Universities Physics Alliance, University of the West of Scotland, Paisley, PA1 2BE, UK

*These authors have contributed equally to the work.

 # Corresponding authors: Dr. Mehdi Jangi, email: m.jangi@bham.ac.uk; Prof. Richard (YongQing) Fu, e-mail: Richard.fu@northumbria.ac.uk

Abstract: This paper investigates vertical droplet jetting using circular surface acoustic wave (CSAW) devices with annular interdigitated transducers (AIDTs) fabricated on ZnO film coated silicon substrate. The surface vibration on the CSAW devices was simulated using finite element analysis and characterised using laser vibrometry. Results showed that focused wave patterns and compact nodal distributions of vibration were formed at the centre of ZnO/Si CSAW device, which is contrast to an anisotropic wave distribution patterns generated by the same pattern of AIDTs fabricated on 128° Y-cut LiNbO₃. Simulation of liquid jetting induced by the isotropically focused

CSAW was performed using coupled Volume of Fluid and Level-Set method. Results showed that a sharp and cylindrical liquid column was generated from the ZnO/Si CSAW device induced by acoustic energy coming from all directions within the plane due to the in-plane isotropic nature of the ZnO thin films. The simulation enabled us to capture the different streaming/jetting processes induced by the anisotropic distributions of acoustic pressure generated by the AIDTs on the 128° Y-cut LiNbO$_3$ CSAW device. The concentrated vertical droplet jetting behaviour from the ZnO/Si CSAW devices was investigated experimentally and supported the simulated results.

Keywords: Focused SAWs, ZnO film, surface acoustic wave, jetting, isotropic.

1. Introduction

Surface acoustic waves (SAWs) excited by applying RF signals to interdigital transducers (IDTs) on a piezoelectric substrate have shown great potential for applications in sensing and microfluidic manipulation in Lab-on-Chip (LOC) devices (Länge et al. (2008), Voiculescu and Nordin (2012), Yeo and Friend (2009), Friend and Yeo (2011), Wixforth (2006), Destgeer and Sung (2015), Luo et al. (2015), Ding et al. (2013)). Various sampling and microfluidic functions including particle manipulation/concentration, acoustic streaming, mixing, pumping, jetting and nebulisation have been reported using the SAW devices made from the bulk substrates such as LiNbO$_3$ (Yeo and Friend (2009), Friend and Yeo (2011), Ding et al. (2012), Ding et al. (2013), Renaudin et al. (2010)) by integrating multi-functions such as surface plasma resonance (Renaudin et al. (2010), Galopin et al. (2007)), dielectrophoresis (Wiklund et al. (2006), Fatoyinbo et al. (2007)), impedimetric sensing (Liu et al. (2013)), phononic crystal superstrates (Wilson et al. (2011)) or electro-wetting on dielectrics (Li et al. (2012)). Recently, thin film based SAW sensors and acoustofluidic devices (Fu et al. (2010), Fu et al. (2017)) have been explored using piezoelectric thin films such as AlN and ZnO deposited onto a range of substrates such as silicon (Fu et al. (2012a), Fu et al. (2012b), Flewitt et al. (2015), Luo et al. (2012), polymers He et al. (2014), Xuan et al. (2015)), and metallic

2

foils (Liu et al. (2015)), for generating CMOS compatible, transparent or flexile/wearable devices.

Among these microfluidic phenomena, droplet ejection or jetting is attractive due to its potential for wide applications in ink-jet printing (Bhattacharjee et al. (2011)), precision microdispensing, patterning of soft biological or fibre synthesis and deposition of biochemical films. To compete with the current methods, SAW devices should be low cost, mass-producible and fully integrated with electronics for control and signal processing systems, and mostly important, generate a highly efficient and concentration jetting effect.

Curved or concentric IDTs have recently been fabricated on LiNbO$_3$ to make focused SAW (FSAW) devices, which are suitable for droplet jetting (Tan et al. (2011), Ai and Marron (2012)). Unlike the conventional straight IDT structures which produce parallel travelling waves, the FSAW devices concentrate the acoustic wave energy into a small focused area, enabling the formation of constructive interference, maximising mechanical displacements in the central focused nodes between the two curved IDTs. Propagation of SAWs on the conventional bulk piezoelectric substrates such as LiNbO$_3$ and quartz, however, exhibits a significant anisotropic effect due to their crystal-cut orientations. Therefore, to obtain efficient focused effect on LiNbO$_3$ using annular IDTs (AIDT) similar to the illustration shown in Fig. 1a, special designs are needed to correct the differences in acoustic velocities in various in-plane crystal orientations, leading to more complex modelling and mask design strategies (Laude et al. (2008)). Such IDT designs are not required for thin film based SAW devices because the deposited piezoelectric films, in principle, have isotropic wave velocities in all surface plane directions (see Fig. 1a, Tigli, and Zaghloul (2008)). Moreover,

3

thin film SAW devices, such as those based on ZnO or AlN, offer advantages of integration capabilities with microelectronics and other technologies. They also have much higher power handling capability and potentially lower failure/damage rates. For example, ZnO SAW devices could withstand high RF powers applied to the IDTs without causing failures of substrate fracture, frequently observed with $LiNbO_3$ SAW devices. However, the formation of vertical droplet jetting using circular surface acoustic wave (CSAW) devices with circular electrodes and the accompanying flows have not been systematically investigated. In this paper, we show that an in-plane isotropic ZnO/Si SAW device with annular IDTs (AIDTs), generates focused SAWs that induce jetting. We provide a systematic study of the mechanisms through both theoretical analysis and experimental characterisation enabling us to characterise the differences in the jetting mechanisms between the CSAW devices fabricated on ZnO/Si and 128° Y-cut $LiNbO_3$.
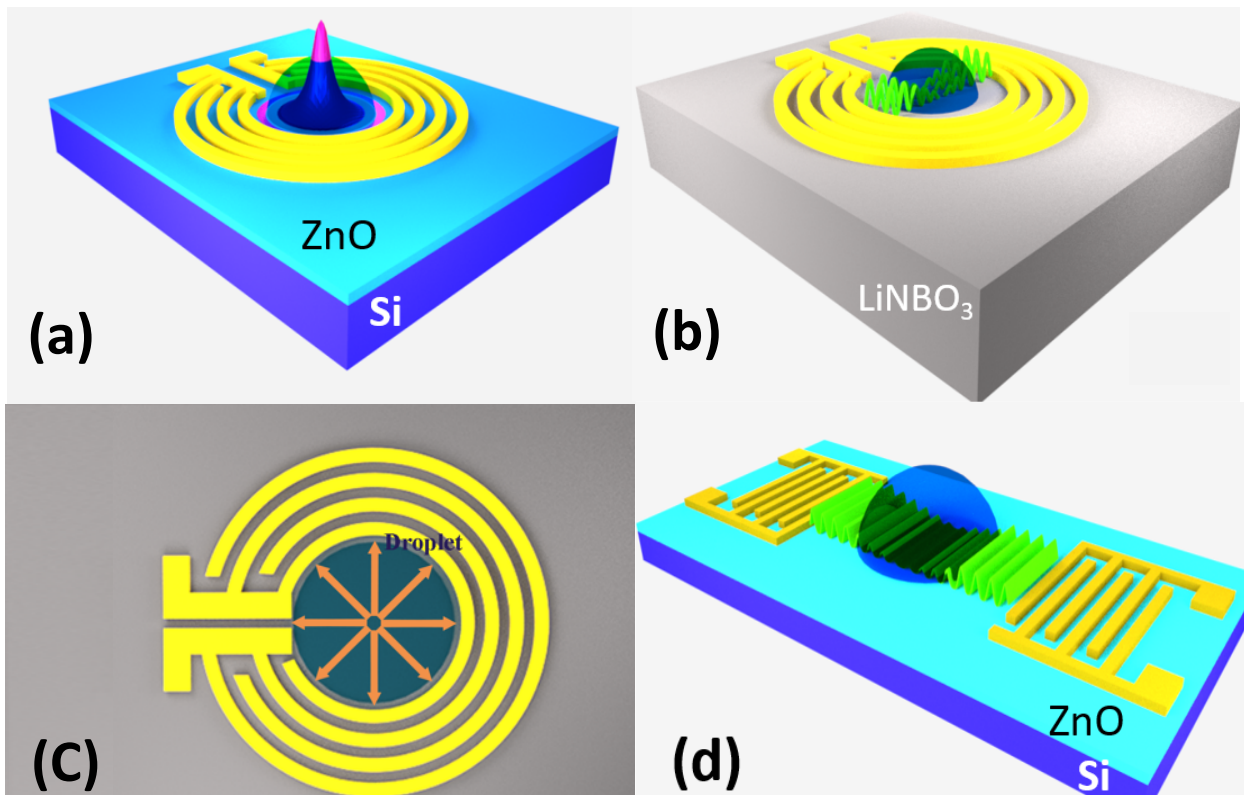
Fig.1. (a) Schematic illustration of circular ZnO/Si CSAW devices with annular IDTs with concentrated acoustic pressure distribution; (c) Microfluidic streaming observed on a CSAW, which occurs inside the droplet and the fluid was driven in circular patterns from the centre to the outside; (b) Schematic of the acoustic wave generation from the CSAW device made of 128° Y-cut LiNbO$_3$ device, showing generation of waves along one direction at a given frequency signal; which is similar to (d) a standing SAW generated by two waves from two straight IDTs.

2. ZnO/Si SAW device: fabrication and characterisation

ZnO films with a thickness of ~3.5 μm was deposited onto silicon (100) substrate using a standard DC magnetron sputter. A Zn target (99.99%) was used with an RF power of 400 W and Ar/O$_2$ flow ratio of 6/12 SCCM (standard cubic centimetre per minute) without intentional substrate heating. During deposition, the gas pressure was ~5 mTorr. X-ray diffraction analysis showed that the film has a strong (0002) orientation. More details of ZnO film deposition and properties can be found from our previous reports (Fu et al. (2012a), Fu et al. (2012b)).

Aluminum IDTs with 150 nm thick were fabricated using a standard sputtering and lift-off process. The AIDTs was consisted of 15 pairs of circular fingers (see Fig. 4(a)) with a wavelength of 400 μm and fabricated on both ZnO/Si and 128° Y-cut LiNbO$_3$ substrates. The frequency responses of the SAW devices were characterized using a network analyser (Agilent Technologies E5071C). The spectra of reflection s-parameter (S$_{11}$) curves for both the ZnO and LiNbO$_3$ CSAW devices are shown in Fig. 2. The SAWs generated on the LiNbO$_3$ ASAW devices have a wide range of resonance frequency peaks, corresponding to the different propagation velocities along the different directions of the crystal, and they can be traced to two main resonant frequencies at around 9.8 and 16.6 MHz with many spurious modes. These two main peaks can be assigned to

5

the acoustic wave velocities of LiNbO₃ in the X-axis and Y-axis. According to this measurement, it is impossible to simultaneously generate waves from all directions by applying with one given frequency, and one frequency could only generate waves along one direction as shown in Fig. 1b. On the contrary, the ZnO CSAW device shows much narrower peak range between 12 to 12.6 MHz (see Fig. 2), demonstrating isotropic wave propagation velocities in the horizontal plane. The peak intensity is lower due to its thin nature (i.e., 3.5 microns thick compared to 500 microns of LiNbO₃ substrate). Some minor ripples along with the main frequency peak were observed for the S_{11} peaks of the ZnO CSAW, probably due to the rough surface nature of ZnO coated device, triple transit effect and leaky bulk waves in silicon, etc (Xuan et al. (2015)).
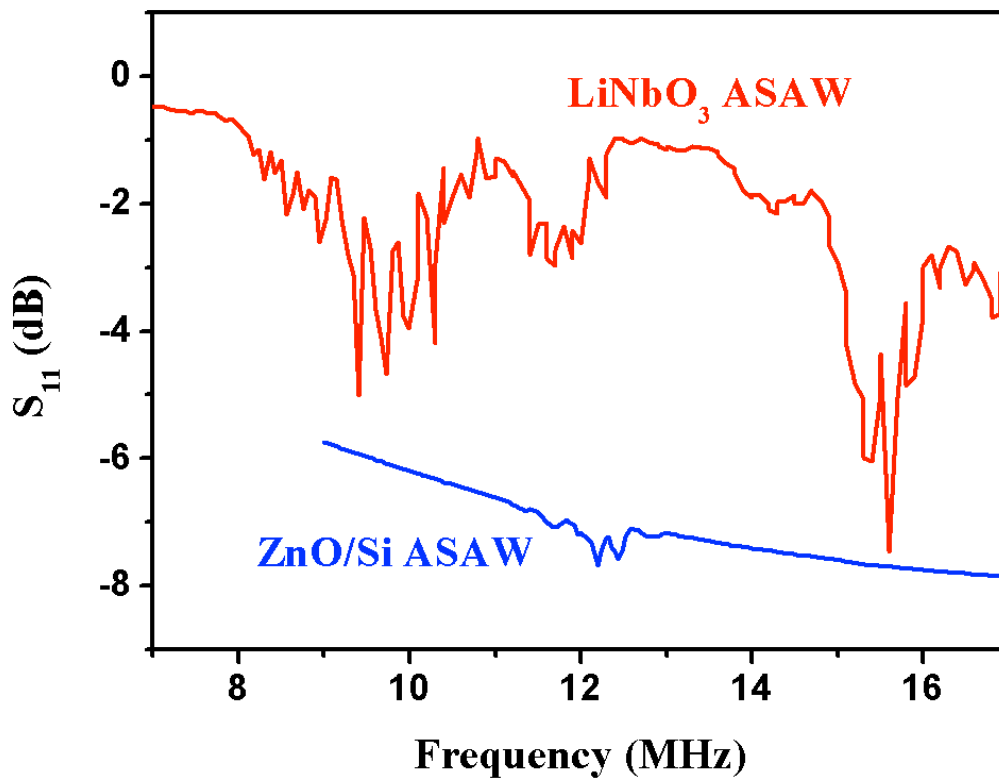

Fig. 2 Reflection performance of ASAW devices with circular patterns on ZnO/Si and LiNbO₃ substrate.

The amplitudes of surface vibrations on both ZnO/Si and LiNbO$_3$ SAW devices were measured using a laser vibrometer (UHF, Polytec GmbH) with a 15 dBm RF excitation at a given frequency. Typical vibration images at a stable condition on the surfaces of both ZnO and LiNbO$_3$ CSAW devices are shown in Fig 3. The surface vibration patterns and the vibration amplitudes on ZnO CSAW devices show an isotropic focusing of the SAWs with a compact nodal distribution (see Figs. 3a and 3b), which is highest at the centre of the ZnO CSAW device. Therefore, it is expected that the waves generated from the ZnO AIDTs will be from all directions, concentrating to the centre of the AIDTs at the resonant frequency.

In contrast, the surface vibration image of LiNbO$_3$ CSAW devices excited at the frequency of 9.8 MHz shows a broad wave propagating along the horizontal direction (Fig. 3(c)), while the displacement in the perpendicular direction is significantly weaker. As shown in Fig, 3(d), a shift of the applied frequency to 16.6 MHz, changed the wave propagation pattern significantly, with a broad wave propagating along the perpendicular direction (Fig. 3(d)), while the displacement in the horizontal direction is weak. Similarly, the surface vibration image of the LiNbO$_3$ CSAW devices excited at the frequency of 12 MHz also show a similar phenomenon. These results demonstrate that the LiNbO$_3$ CSAW devices show the significant anisotropic wave propagation, as illustrated in Fig. 1b.
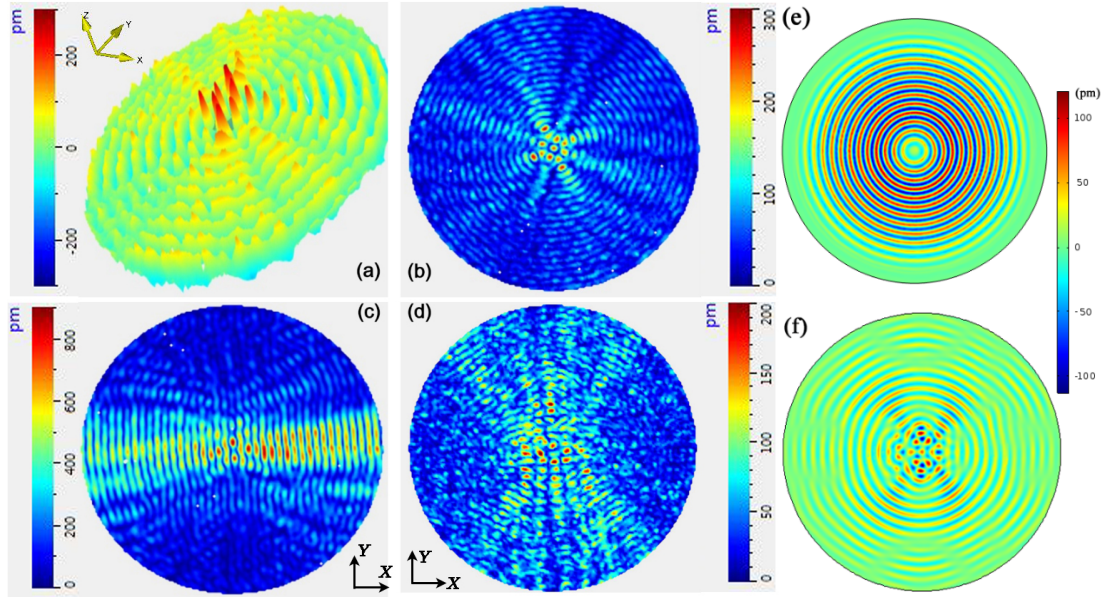
Fig. 3. Surface vibration images with the power of 15 dBm obtained using a laser vibrometer. (a) and (b) surface vibration of ZnO CSAW devices excited at the frequency of 12.3 MHz, demonstrating the isotropic surface vibration in the plane with a compact nodal distribution; (c) surface vibration of LiNbO$_3$ CSAW devices excited at the frequency of 9.5 MHz; (d) surface vibration of LiNbO$_3$ CSAW devices excited at the frequency of 16.6 MHz. Both (c) and (d) demonstrate the anisotropic surface vibration in the horizontal plane. (e) and (f) Comsol simulation results of distribution of wave vibration amplitudes for the CSAWs on a ZnO/Si device and a LiNbO$_3$ SAW device, respectively.

Simulation based on finite element analysis was carried out using COMSOL Multiphysics 5.2a software to investigate the vibration and the wave propagation of CSAWs mode based on ZnO/Si and LiNbO$_3$. The AIDTs consisted of 15 pairs of circular fingers with a wavelength of 400 μm on both the ZnO/Si and the 128° Y-cut LiNbO$_3$ substrates. In these systems, the wave energy dissipates into the bulk of the material and the reflection of the acoustic waves from the boundaries of the substrates are not negligible, therefore, a 3-dimension cylinder model with a height of 3 times the wavelength was used in this simulation. All the surfaces of the cylinder model except for the top surface were set as low-reflecting boundaries. One pad of the IDTs was connected to an input

sinusoidal voltage ($V=V_0\times\sin(2\times PI\times f_0\times t)$), and the other pad of IDTs was electrical grounded. Using the physical field interface of the piezoelectric effect, we investigated the surface vibration of the cylinder model with time-dependent analysis method when the sinusoidal voltage with different frequencies was applied on the AIDTs of ZnO/Si and 128° Y-cut LiNbO$_3$ substrates. Fig. 3(e) shows the surface vibration displacement in the Z direction for the ZnO/Si CSAW device for a frequency of 12.3 MHz from the simulation results, confirming that the uniform and concentrated vibration patterns are obtained experimentally (Fig. 3(b)). Similarly, Fig. 3(f) shows that the surface vibration displacement (z direction) for the 128° Y-cut LiNbO$_3$ CSAW device at 16.6 MHz is much stronger along the Y direction than along X direction, confirming the anisotropic surface vibration in Y-cut LiNbO$_3$ (Fig. 3(d)).

For microfluidic testing, the SAW devices were mounted onto a bulk-aluminium alloy holder acting as a heat sink. The testing areas were spin-coated with a layer (~200 nm) of hydrophobic CYTOP (Asahi Glass Co., Ltd.). Drops of de-ionized water (2 μL) were placed at the centre of the AIDTs. Radio frequency (RF) input signals were applied using a signal generator (Marconi 2024) and RF power amplifier (75A250, Amplifier Research). The droplet streaming and jetting behaviours were recorded using a high speed video camera (Photron XLR Express). Experimental observation clearly shows the droplet streaming patterns generated in the fluid by SAWs propagating at a frequency of 12.3 MHz (RF power of 0.5 W) onto a ZnO/Si CSAW device. The fluid flows from the centre of the droplet upwards and radially to surrounding circular edges,

forming continuous flow patterns similar to those shown in Fig. 1(c), which agree with the pressure distribution into a focused point, generated by the surface vibration pattern.

3 Experimental jetting behaviours from the ZnO/Si and LiNbO$_3$ CSAWs

Fig. 4 shows the high-speed images captured from a movie taken at 500 frames s^{-1} showing the jetting phenomena of 2 μL droplets at different stages using two types SAW devices. When a droplet is put in the centre of the AIDTs, with the frequency of ~12.2 MHz and an RF power of 12 W applied on ZnO/Si CSAW device, acoustic streaming occurred inside the droplet and the fluid was driven in a circle patterns from centre upwards to outside radiantly. At a high power, a large concentrated acoustic energy is dissipated into the droplet, resulting in an inertial pressure in the centre of the fluid. This overcomes surface tension of the liquid and produces a coherent, thin and sharp cylindrical liquid column in the centre of the liquid drop as shown in Fig. 4(a). The energy from all directions is concentrated, resulting into a thin beam of the cylindrical liquid column. Finally, the cylindrical liquid column is ejected continuously with nearly the same diameter (see Fig. 4a. The experimentally obtained jetting behaviour precisely follows the jetting mechanisms from the simulation results shown in Fig. 4. Clearly using the ZnO/Si CSAW device proposed in this study, controllable, nozzle-free liquid jets by isotropic focusing surface acoustic wave energy into the water droplet can be realized easily with a simple fabrication process.
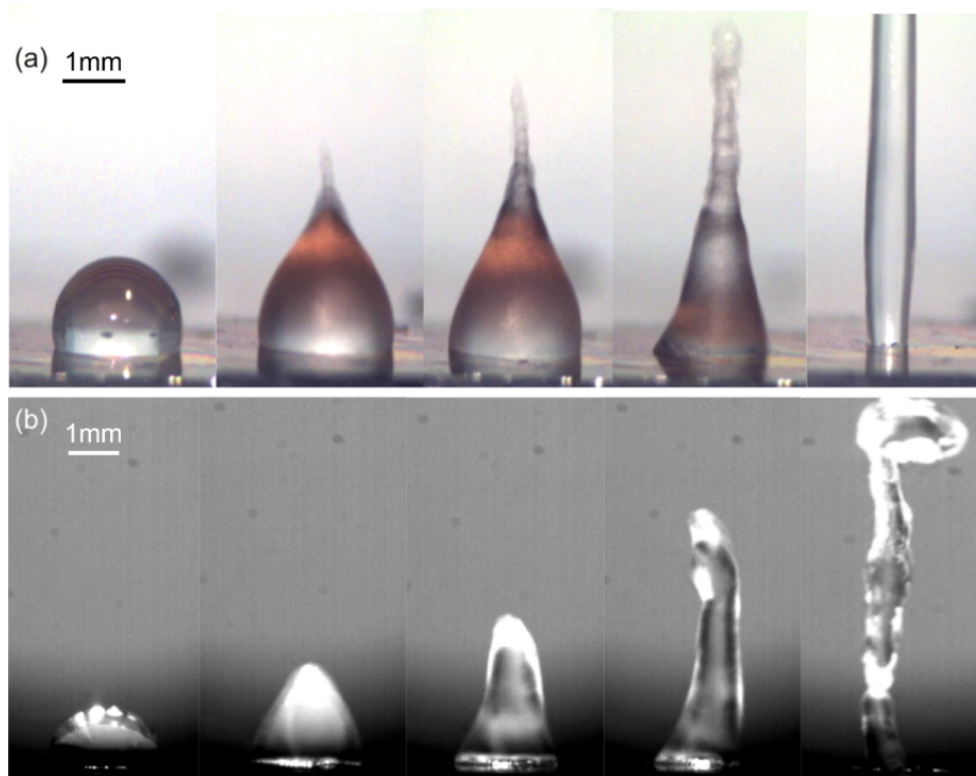
Fig. 4 Images of 2 µL droplet jetting phenomenon induced by the CSAW captured from a movie taken at 1000 frames s^{-1}. (a) AIDT on ZnO/Si SAW device (b) AIDT on 128° Y-cut LiNbO$_3$ SAW device.

A similar elongated liquid column was also reported to form on superhydrophobic treated surface with focused acoustic waves (Darmawan and Byun (2015)), in which case due to the very narrow contact area, the radiation profile is concentrated on a narrow trajectory to the apex of the droplet. A sharp jetting pinching point was formed at the apex of the droplets rather than at the droplet pinning point and inertial body force was mostly concentrated on the apex of the droplet. An elongated liquid column is sharp and narrow under this small jet radius. However, our circular jetting pattern is not due to this superhydrophobic effect, as clearly the contact angle for all the droplets are only about 90 to 95 degrees.

11

For comparison, the jetting behaviour of the LiNbO₃ CSAW device is shown Fig. 4(b) at an RF power of 4.5 W at a frequency of 9.5 MHz, and the images were obtained from a movie taken at 1200 frames s⁻¹. Due to the anisotropic nature, at a given frequency, the SAW energy is actually launched from two broad sides of the droplet, thus the droplet is pushed up from both sides by the opposing waves based on the Rayleigh angle (θ_R), as illustrated in Fig. 1(d). This affects the shape of the jet and does not result in a highly concentrated thin liquid column in the centre of the drop, as shown in Fig. 4(c), which has the similar streaming mechanisms induced by a stranding wave LiNbO₃ FSAW devices Luo et al. (2009).

4 Mathematical model and CFD modelling

CFD calculations/simulations were performed to predict the mechanism of the concentrated flow, droplet deformation and eventually the jetting phenomenon induced by the annular ZnO/Si SAW device. The flow calculations consider two-phase flows and interfacial phenomena such as surface tension and the break up processes of a jet. The governing equation for such a flow system in the absence of evaporation and phase change among phases is:

$$\frac{\partial}{\partial t}(\rho \boldsymbol{U}) + \nabla.(\rho \boldsymbol{UU}) = -\nabla p + \nabla.\boldsymbol{\tau} + \rho \boldsymbol{g} + \boldsymbol{f}_\sigma + \boldsymbol{f}_{SAW} \tag{1}$$

where symbols in bold are used for vector and tensor variables. In this equation $\boldsymbol{U}$ is the velocity and $\boldsymbol{g}$ is the gravitational acceleration vector; $\boldsymbol{f}_\sigma$ and $\boldsymbol{f}_{SAW}$ are the forces due to the surface tension and surface acoustic waves, respectively; ρ is the density of the liquid; p is the pressure; and $\boldsymbol{\tau}$ is the viscous stress tensor defined by $\tau_{ij} = \mu(\frac{\partial U_j}{\partial x_i} + \frac{\partial U_i}{\partial x_j})$. To perform the modelling, an expression for $\boldsymbol{f}_\sigma$ and $\boldsymbol{f}_{SAW}$ is required.

In this study we used a similar form of expression proposed by Shiokawa et al (1989). for the acoustic force f_{SAW} induced by ZnO/Si ASAW device, as:

$$f_{SAW} = \rho(1 + \alpha_1^2)^{\frac{3}{2}} A^2 \omega^2 k \exp(-2[kr + \alpha_1 kz]) \tag{2}$$

where r and z are the radial and axial positions based on an origin of the coordinate at the centre of the liquid region on the surface. α_1 is the attenuation coefficient, and k is the wave number which are two device dependent parameters. A is the SAW amplitude, ω is the angular frequency of the wave. In this study, the acoustic force follows a distribution similar to that illustrated in Fig. 1b. The above expression ensures the maximum of f_{SAW} at the centre of the interface between droplet and solid surface, and it is exponentially decreasing in space. The exact values for the wave parameters α_1, k, A and ω induced by the current device are not known, nonetheless they appear as a parameter $A^2 \omega^2$ in Eq. 2, which is an indication of the induced SAW's power. Therefore, we treated the $A^2 \omega^2$ as a model tuning parameter and performed several simulations with various $A^2 \omega^2$ to achieve a close match between the simulation results and experiments. Following Alghane 2013, the value of α_1 was selected to be 2.47, and k was varied between 1384 to 2768.

We used a volume of fluid (VOF) approach to obtain the density ρ and viscosity μ as below:

$$\rho = \rho_l \alpha + \rho_g (1 - \alpha) \tag{3}$$

$$\mu = \mu_l \alpha + \mu_g (1 - \alpha) \tag{4}$$

where α is the liquid volume fraction at each point, and the subscripts 'l' and 'g' indicate the liquid and gas phases, respectively. The variable α is unity in the liquid phase and zero in the gas phase, and evolves by advection as:

13

$$\frac{\partial \alpha}{\partial t} + \nabla . (\boldsymbol{U}\alpha) = 0 \qquad (5)$$

The surface tension $\boldsymbol{f}_\sigma$ can be calculated from $\boldsymbol{f}_\sigma = \sigma\kappa\nabla\alpha$, where σ is surface tension coefficient of the liquid in the gas, and κ is the curvature of the interface obtained from:

$$\kappa = -\nabla.\frac{\nabla\alpha}{|\nabla\alpha|} \qquad (6)$$

Since the definition of α is a discontinuous step function of the gradient of α at the interface, the curvature of the interface is difficult to calculate accurately Sussman and Puckett (2000), Darmawan and Byun (2015). In practice, the outcome of the numerical solution of the advection equation 5 is a continuous function that is varied from unity to zero near the interface continuously. To obtain a sharp interface yet a smooth transition in the physical properties across the interface, the Level-Set (LS) method has been coupled with the VOF. Here we use a coupling approach which was proposed by Sussman and Puckett (2000). In this approach, a LS field ϕ is introduced where the iso-surface $\phi=0$ defines the interface position. The value of ϕ is positive in a liquid phase whereas it is negative in a gas phase. At each CFD time step, it is assumed that the interface position is at $\alpha = 0.5$; therefore, the LS field is initialised as:

$$\phi_0 = (2\alpha - 1).\Gamma \qquad (7)$$

where $\Gamma = 0.75\Delta x$, which is a small non-dimensional number whose value depends on the mesh size Δx. The initialised function ϕ_0 is a sign function which is positive in the liquid phase and negative in the gas phase. ϕ_0 is derived by solving the re-initialisation equation:

$$\frac{\partial \phi}{\partial \tau} = S(\phi_0)(1 - |\nabla\phi|) \qquad (8)$$

14

here, τ is an artificial time step. The solution of equation 8 converges to a signed distance function

when $|\nabla\phi|=1$. The interface based on ϕ is much smoother and sharper compared to that based on

the volume fraction α Sussman and Puckett (2000). Subsequently, the curvature at the interface

can be determined as $\kappa(\phi) = -\nabla.\frac{\nabla\phi}{|\nabla\phi|}$, and the surface tension force can be calculated from $f_\sigma =$

$\sigma\kappa(\phi)\delta(\phi)\nabla\phi$. In the correlation for the surface tension, $\delta(\phi)$ is the Dirac function and can be

obtained from:

$$\delta(\phi) = \begin{cases} 0 & |\phi| > \epsilon \\ \frac{1}{2\epsilon}\left(1 + \cos\left(\frac{\pi\phi}{\epsilon}\right)\right) & |\phi| \leq \epsilon \end{cases} \tag{9}$$

where ϵ is the interface thickness that is chosen as $\epsilon = 0.75\Delta x$ Sussman and Puckett (2000).

Similarly, the physical properties are defined using a smooth Heaviside function H:

$$\rho(\phi) = \rho_g + (\rho_l - \rho_g)H(\phi) \tag{10}$$

$$\mu(\phi) = \mu_g + (\mu_l - \mu_g)H(\phi) \tag{11}$$

where

$$H(\phi) = \begin{cases} 0 & |\phi| \quad \epsilon \\ \frac{1}{2}\left[1 + \frac{\phi}{\epsilon} + \frac{1}{\pi}\sin\left(\frac{\pi\phi}{\epsilon}\right)\right] & |\phi| \leq \epsilon \\ 1 & |\phi| > \epsilon \end{cases} \tag{12}$$

The governing equations and the level set equations were solved using OpenFOAM-4.x.

5 Mechanism of jetting by SAW devices

Simulation has been performed for a droplet of water at room temperature with an initial droplet

radius R of 1 mm. The computational domain is a rectangular box with a dimension of

$5R \times 5R \times 20R$. A fully Cartesian mesh was generated, and a local mesh refinement strategy was

employed to refine the mesh in the liquid region and near the interface. The local refinement was

15

extended along z-direction in the entire jetting region. In total, approximately 2 million CFD cells were required to resolve the flow inside the droplet and capture the droplet's deformation and its following jetting stream.

Figure 5 shows snapshots of CFD simulation results at iso-surface $\alpha=0.5$, which is used to identify the interface position and its evolutions in time. The interval between these snapshots is 2 ms. As it can be seen, the modelling approach based on the VOF-LS method can simulate the droplet (in Fig. 5a) jetting process from droplet deformation in Fig. 5b to the development of the instabilities across the tip of the deformed droplet in Fig. 5c to the jetting of the liquid Fig. 5d and the growth of the instabilities and break-up of droplet in Fig. 5e.
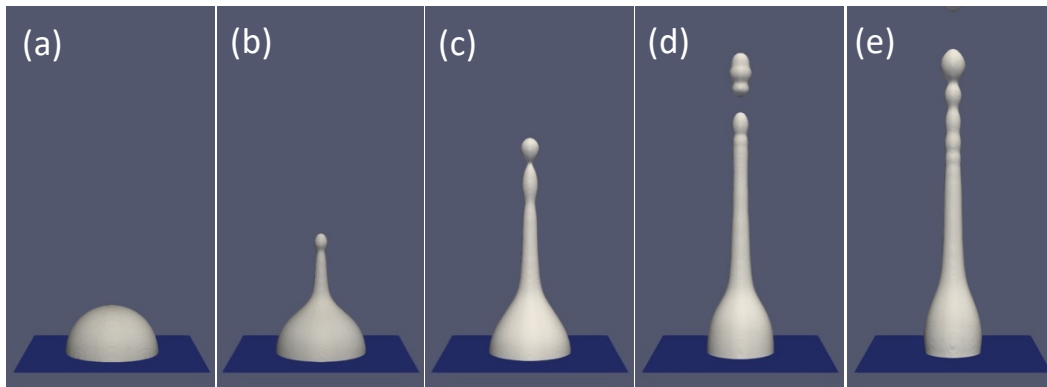

Fig. 5. Snapshots of the iso-surface $\alpha = 0.5$ for droplet jetting phenomenon induced by a circular SAW based on the CFD results; the interval between these snapshots is 2 ms, $\alpha_1 = 2.47$, and $k=2768$.

Figure 6 shows the jet penetration height (JPH) as a function of time for three different powers. The symbols in this figure represent the measured JPH that obtained by processing high speed images captured by the CCD camera, whereas the lines are the JPH based on the simulation results. The agreement between the experiments and simulation results are remarkable in all cases. As it can be seen, at the lowest power, the induced energy by the SAWs has only generated a droplet

16

deformation in vertically direction rather than a significant jetting stream. As the power is increased, a droplet jetting is formed and the tip of the jet reaches to its peack at almost 3 mm (three time the intial droplet diameter), before the gravitational force can supress the jetting processes and reverse the flow direction. At the highest power, the energy is large enough to generate a full droplet jetting and atomisation, similar to those cases that are shown in Figs. 4 and 5.
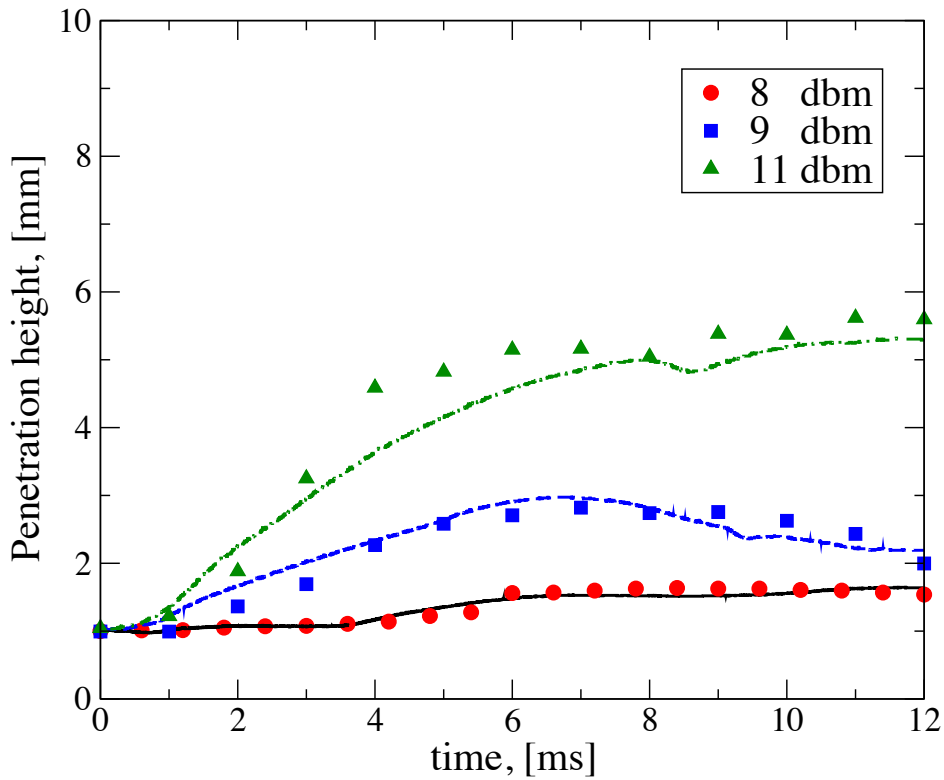

Fig. 6. Time history of the jet penetration height at three different SAWs powers (symbols represent the experimental measurements and lines are from calculations).

The mechanism of the full jetting is further examined in Figs. 7 and 8. Fig. 7 shows the time history of the LS function ϕ. This variable can be used to identify the evolution of the liquid-gas interface. By definition (see Eq. 7), a positive value of ϕ refers to the liquid and a negative value to the gas phase; the interface is then at $\phi = 0$. In this figure, velocity vectors are also shown to help to visualise the flow patterns in a droplet jetting phenomenon.
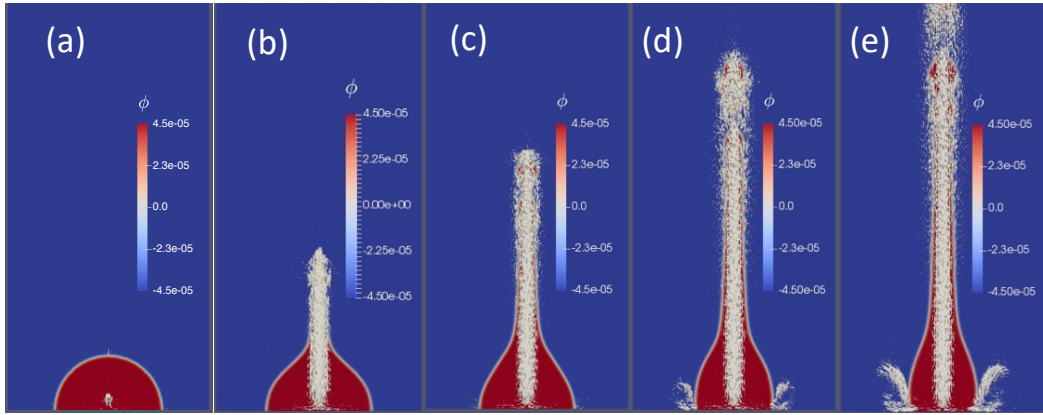
Fig. 7. CFD Snapshots of ϕ (see Eq. 7), overlaid by velocity vectors during the first 8 ms of the jetting process; the interval between these snapshots is 2 ms, α_1= 2.47, and k=2768.

Results showed that the droplet maintains its hemi-spherical shape, similar to that shown in Fig. 7a for approximately 1 ms after it is subjected to a SAWs force. During the next 1 ms, visible deformations across the interface of the droplet occur, and the deformed interface quickly developed into a jetting stream as shown in Figs. 7b to 7e. Velocity vectors confirm that the jetting is a consequence of a strong vertical momentum of the flow that is induced by the circular focused SAWs (see Eq. 2 and the discussion therein). The streaming velocities of liquid in these snapshots exceed 4 m/s.

An interesting feature in Fig. 7 is the formation of an annular vortex in gas phase across the boundary of the droplet and in the vicinity of the solid surface. As it can be seen, the annular vortex is not formed until 4 ms from the start of calculations in Fig. 7d. The formation of this vortex structure is due to the droplet shrinkage after 4 ms. Such shrinkage at the interface is due to the vertical jetting stream to supply the liquid mass that is ejecting from the surface outward.

18

Another interesting observation in a droplet jetting phenomenon is the creation of instabilities across the surface of droplet which can potentially lead to the breakup of the jet. Here we examine this process in more details. Fig. 8 shows the snapshots of pressure distribution as a function of time. The interface position is shown by an iso-contour of $\alpha = 0.5$. Immediately after the SAW pressure is applied, a high-pressure has been generated at the centre of the droplet as seen in Fig. 8a. This force generates a vertical stream from the surface toward the free surface of the droplet as it can be seen in Figs. 7a to 7e. Especially, in the time history of the velocity vectors shown in Figs. 7a and 7b, it can be seen that this vertical streaming requires time before it is strong enough to deform the droplet interface. With a small SAW force, the vertical stream is diverted when it reaches the tip of the droplet at the interface, which is due to the effect of the surface tension force at the free surface of droplet. The combination of the actions of the SAWs and surface tension forces create a re-circulation inside the droplet in which the energy supplied to system by the SAWs is dissipated by the viscous effects.
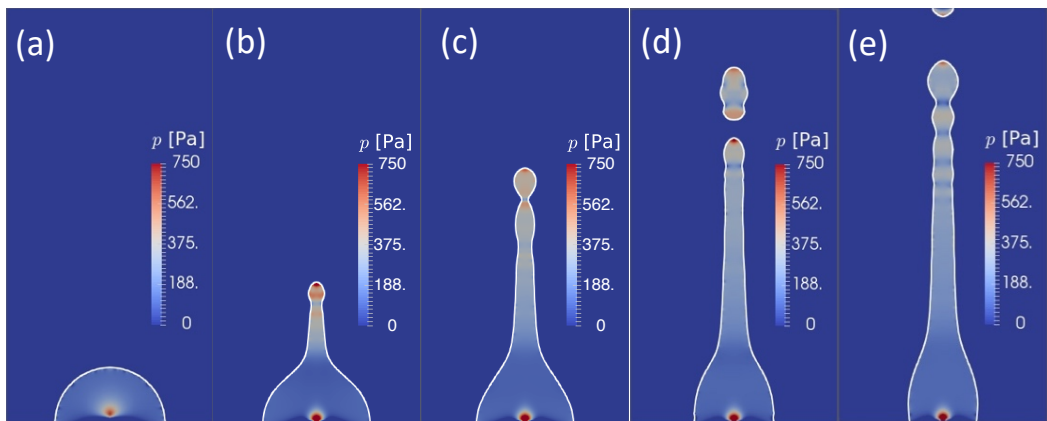

Fig. 8. CFD Snapshots of pressure during the first 8 ms of the jetting process; the solid white line indicates the position of the interface, $\alpha_1 = 2.47$, and $k=2768$.

On the other hand, when the SAW pressure is large enough to generate a strong enough vertical stream with a momentum that cannot be sustained by the surface tension force at the interface, the free surface of the droplet starts to be deformed outward. Fig. 7b is a typical illustration of such conditions in which an initially hemi-spherical droplet free surface has been deformed into a pre-jetting flow. Several scenarios such as droplet interface oscillation, jetting and ejection can occur in this instance depending on the ratios among (a) SAW force that induces the momentum; (b) viscous force that dissipates the energy supplied by the SAWs to the system; and (c) the surface tension force that diverts the direction for the momentum at the interface. Depending on the power applied to the IDTs, all these scenarios could happen. Here we only focused on the mechanism of the instabilities occurring across a jetting droplet. The surface tension is proportional to the curvature of the surface; e.g., $f_\sigma = \sigma\kappa\nabla\alpha$. Therefore, the surface tension at the tip of the deformed droplet increases as a result of increasing the curvature at the tip of the liquid jet, as can be seen in the second snapshot. The jetting can be potentially suppressed if the increased surface tension force can balance the vertical streaming momentum. However, this is not the case if the applied SAWs are large enough to continuously push forward the droplet surface as seen in the subsequent snapshots.

The deformation of the droplet surface also drives the internal pressure of a droplet, which is a function of its free surface curvature. Therefore, at the tip of the jet where the curvature is large, the pressure is high (Fig. 8b). Similarly, across the jet in the region where the pressure is low, the curvature of the interface decreases, and this low-pressure region can also be identified in Fig. 8b.

20

Such high-pressure and low-pressure regions occur across the jet, and in turn trigger the local deformations and instabilities, known as Plateau-Rayleigh instabilities. These instabilities can develop into a jet breakup process as seen in the last two snapshots as shown in Figs. 8d and 8e.

The mechanism of jetting from the 128° Y-cut LiNbO$_3$ SAW device is the same as that with ZnO, to a large extent. Fig. 9 shows the time history of the simulation results at iso-surface α=0.5 (on the top row), and the snapshots of ϕ (on the bottom). Results are comparable with the experimental images in Fig. 4b. In particular, the tip of the jet in this case is much broader than the tip of the jet in Figs. 5 and 7, which is consistent with the experimental obsevrations. The breakup of the jet, however, was not captured properly in the simulation (see Fig. 4e). The reason is that the dynamic of the contact angle with LiNb O$_3$ device at the onset of breakup involve rapid changes that was not possible to capture with current numerical approach. More sophisticated contact angle model would be required in order to reproduce the experimental results shown in the last snapshot of Fig. 4b.
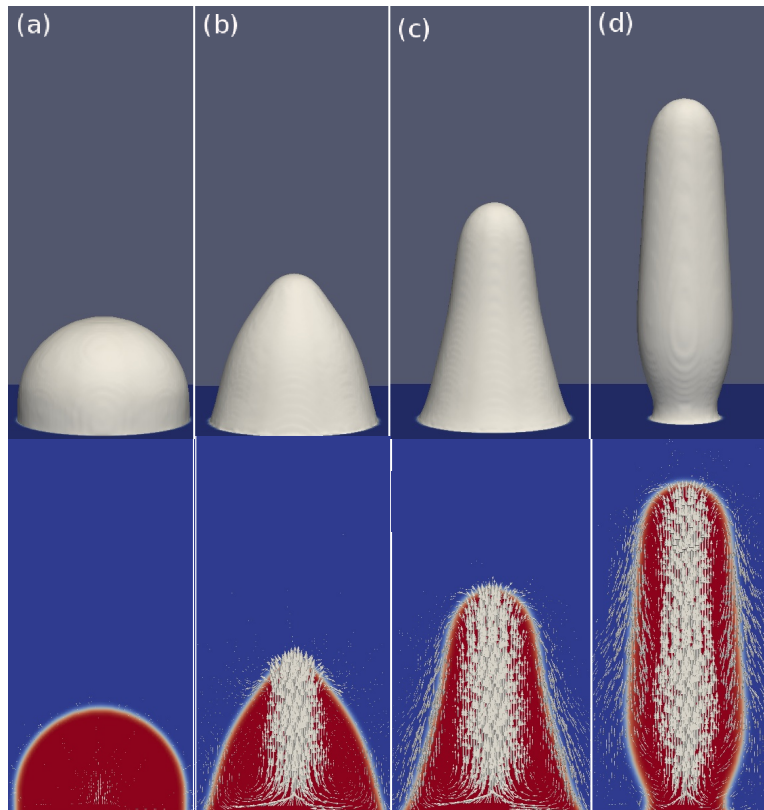
Fig. 9. Snapshots of the iso-surface $\alpha = 0.5$ for droplet jetting phenomenon induced by a circular SAW based on the CFD results (on the top row), and ϕ overlaid by velocity vectors during the first 8 ms of the jetting process (on the bottom); the interval between these snapshots is 2 ms, $\alpha_1 =$ 2.47, and $k=1384$.

6. Conclusions

This paper clarified the jetting mechanism from an ASAW on a ZnO thin film surface which enables a concentrated and compact nodal distribution of the SAW at the centre of the annular electrodes. Using this ZnO ASAW, a controllable, nozzle-free concentrated thin liquid jet process have been generated by focusing the SAW energy into the centre of the water drops. This is in contrast to the anisotropic wave distribution generated from a 128º Y-cut LiNbO3 ASAW device, and does not result in a highly concentrated thin liquid column. The isotropic properties of the ZnO thin film enable a simple and straightforward design process to realize a focused wave vibration

pattern, while complex modelling is required for design IDT shapes of the bulk anisotropic crystals such as LiNbO$_3$.

Acknowledgement

References

Ai Y., and Marrone B.L. 2012, Droplet translocation by focused surface acoustic waves. Microfluidics and nanofluidics, 13(5):715-722.

Alghane 2013, Surface acoustic wave streaming in a microfluidic system, PhD thesis, Hariot Watt University.

Bhattacharjee K.B., McDonnell A. G., Prabhakar R., Yeo L. Y., Friend J.R. 2011, Extensional flow of low-viscosity fluids in capillary bridges formed by pulsed surface acoustic wave jetting, New J. of Phys. 13 023005 1367-2630

Darmawan, M. and Byun D. 2015, Focused surface acoustic wave induced jet formation on superhydrophobic surfaces. Microfluidics and Nanofluidics, 18(5-6): 1107-1114.

Ding X., Li P., Lin S., Stratton Z.S. , Nama N., Guo F., Slotcavage D., Mao X., Shi J., Costanzo F., Luo J.T., Pan F., Fan P., Zeng F., Zhang D.P., Zheng H.Z., Liang G. X. 2012, Cost-effective and high frequency surface acoustic wave filters on ZnO:Fe/Si for low-loss and wideband application, Applied Physics Letters, 101 172909.

Ding X., Li P., Lin S-C S., Stratton Z.S., Nama Ni., Guo F., Slotcavage D., Mao X., Shi J., Costanzoa F., Huang T. J., 2013. Surface acoustic wave microfluidics, Lab. Chip. 13, 3626-3649

Fatoyinbo HO, Hoettges KF, Reddy SM, Hughes MP, 2007. An integrated dielectrophoretic quartz crystal microbalance (DEP-QCM) device for rapid biosensing applications Biosens Bioelectron. 23, 225-232.

Flewitt A.J., Luo J.K., Fu Y.Q., Garcia-Gancedo L., Du X.Y., Lu J., Zhao X., Iborra E., Ramos D. M., Milne W.I., 2015. ZnO Based SAW and FBAR devices for Bio-Sensing applications, Journal of Non-Newtonian fluid mechanics 222, 209-216

Friend J. R., Yeo L. Y., 2011. Microscale acoustofluidics: Microfluidics driven via acoustics and ultrasonics Rev. Modern Phys. 83, 647-704 .

Galopin E., Beaugeois M., Pinchemel B., Camart J., Bouazaoui M., Thomy V, 2007, SPR biosensing coupled to a digital microfluidic microstreaming system, Biosens. & Bioelectron. 23, 746-750.

Fu YQ, Luo JK, Du XY, Flewitt AJ, Li Y, Walton AJ, Milne W.I., 2010. Recent developments on ZnO films for acoustic wave based bio-sensing and microfluidic applications: a review. Sens. Actuat. B, 143: 606.

Fu Y.Q. , Garcia-Gancedo L., Pang H.F., Porro S., Gu Y.W., Zu X. T., Placido F., Wilson J., Flewitt A.J., Milne W.I., 2012a. Microfluidic of ZnO/nanocrystalline diamond surface acoustic wave devices, Biomicrofluidics 6, 013864.

Fu Y.Q., Li Y., Zhao C., Placido F., Walton A.J., 2012b. Surface acoustic wave nebulisation based on nanocrystalline ZnO film, Appl. Phys. Lett. 101, 194101.

Fu Y.Q., Luo J.K., Nguyen N.T., Walton A.J., Flewitt A.J., Zu X.T, Li Y., McHale G., Matthews A., Iborra E., Du H. , Milne W.I., 2017. Advances in piezoelectric thin films for acoustic biosensors, acoustofluidics and lab-on-chip applications, Prog. Mater Sci. 89, 31-91.

Ghulam Destgeer and Hyung Jin Sung, 2015. Recent advances in microfluidic actuation and micro-object manipulation *via* surface acoustic waves , Lab. Chip. 15, 2722-2738

He X.L., Guo H.W., Chen J.K., Wang W.B., Xuan W.P., Xu Y., Luo J.K., 2014. Bendable ZnO thin film surface acoustic wave devices on polyethylene terephthalate substrate, Appl Phys Lett 104: 213504.

Laude V., Gerard D., Khelfaoui N., Jerz-Hanckes C.F., Benchabane S., Khelif A., 2008.

Subwavelength focusing of surface acoustic waves generated by an annular interdigital transducer. Applied Physics Letters 92(9), 094104.16.

Länge K., Rapp B.E., Michael Rapp, 2008. Surface acoustic wave biosensors: a review. Anal Bioanal Chem (2008) 391:1509–1519

Liu Y., Li Y., Al-Hady A.M., Zhao C., Du J. F., Liu Y., Fu Y.Q., 2015. Flexible acoustofluidics based on ZnO film coated aluminium foil, Sens. Actuat. B, B 221 230–235.

Li Y., Fu Y.Q., Brodie S., Mansuor A., Walton A., 2012. Enhanced microdroplet splitting, concentration, sensing and ejection by integration of electrowetting-on-dielectrics and surface acoustic wave, Biomicrofluidics 6, 012812.

Liu F., Li F., Nordin A.N., Voiculescu I., 2013, A Novel Cell-Based Hybrid Acoustic Wave Biosensor with Impedimetric Sensing Capabilities, Sens. 13, 3039-3055.

Luo J.K. , Fu Y.Q., Li Y., Du X.Y., Flewitt A.J, Walton A.J. , Milne W.I., J.,2009, Moving-part-free microfluidic systems for lab-on-achip, Micromech. Microeng., 19, 054001.

Renaudin A., Chabot V., Grondin E., Aimez V., Charette P.G., 2010, Lab Chip 10, 111-115. Voiculescu L., Nordin A.N., 2012, Acoustic wave based MEMS devices for biosensing applications, Biosensors and Bioelectronics 33, 1–9.

Shiokawa, S., Matsui, Y., Ueda, T., 1989. Liquid streaming and droplet formation caused by leaky Rayleigh waves. IEEE Ultrason. Symp. 1 643–646

Sussman, M., Puckett, E.G., 2000. A coupled level set and volume-of-fluid method for computing 3d and axisymmetric incompressible two-phase flows. J. Comput. Phys. 162, 301–337.

Tan M.K., Friend J. R., Yeo L., 2009. Interfacial Jetting Phenomena Induced by Focused Surface Vibrations , Phys. Rev. let., 103 (2009) 024501.

Tigli, O. and M.E. Zaghloul, 2008, Design, modeling, and characterization of a novel circular surface acoustic wave device. Sensors Journal, IEEE 8(11): p. 1807-1815.

Wixforth A., 2006. Acoustically Driven Programmable Microfluidics for Biological and Chemical Applications J. of the Association for Laboratory Automation, 11 (6), 399-405 (2006).

Wiklund N, Gunther C, Lemor R, Jager M, Fuhr G, Hertz HM, 2006. Ultrasonic standing wave manipulation technology integrated into a dielectrophoretic chip, Lab-on-Chip 6,1537-1544.

Wilson R., Reboud J., Bourquin Y., Neale S.L. , Zhang Y., Cooper J. M., 2011, Phononic crystal structures for acoustically driven microfluidic manipulations, Lab. Chip. 11, 323–328.

Xuan W., He X., Chen J., Wang W., Wang X., Xu Y., Xu Z., Fu Y.Q., Luo J., 2015. High sensitivity flexible Lamb-wave humidity sensor with graphene oxide sensing layer, Nanoscale 7 (16) 7430-7436.

Yeo L.Y. and Friend J.R., 2009. Ultrafast microfluidics using surface acoustic waves, Biomicrofludics, 33, 012002.